

Fast Cloud Adjustment to Increasing CO₂ in a Superparameterized Climate Model

Matthew C. Wyant¹, Christopher S. Bretherton¹, Peter N. Blossey¹, and Marat Khairoutdinov²

¹Department of Atmospheric Sciences, University of Washington, Seattle, WA, USA

²School of Marine and Atmospheric Sciences, Stony Brook University, Stony Brook, NY, USA

Manuscript submitted 8 July 2011, revised 10 Jan 2012

Two-year simulation experiments with a superparameterized climate model, SP-CAM, are performed to understand the fast tropical (30S-30N) cloud response to an instantaneous quadrupling of CO₂ concentration with SST held fixed at present-day values.

The greenhouse effect of the CO₂ perturbation quickly warms the tropical land surfaces by an average of 0.5 K. This shifts rising motion, surface precipitation, and cloud cover at all levels from the ocean to the land, with only small net tropical-mean cloud changes. There is a widespread average reduction of about 80 m in the depth of the trade inversion capping the marine boundary layer (MBL) over the cooler subtropical oceans.

One apparent contributing factor is CO₂-enhanced downwelling longwave radiation, which reduces boundary-layer radiative cooling, a primary driver of turbulent entrainment through the trade inversion. A second contributor is a slight CO₂-induced heating of the free troposphere above the MBL, which strengthens the trade inversion and also inhibits entrainment. There is a corresponding downward displacement of MBL clouds with a very slight decrease in mean cloud cover and albedo.

Two-dimensional cloud-resolving model (CRM) simulations of this MBL response are run to steady state using composite SP-CAM simulated thermodynamic and wind profiles from a representative cool subtropical ocean regime, for the control and 4xCO₂ cases. Simulations with a CRM grid resolution equal to that of SP-CAM are compared with much finer resolution simulations. The coarse-resolution simulations maintain a cloud fraction and albedo comparable to SP-CAM, but the fine-resolution simulations have a much smaller cloud fraction. Nevertheless, both CRM configurations simulate a reduction in inversion height comparable to SP-CAM. The changes in low cloud cover and albedo in the CRM simulations are small, but both simulations predict a slight reduction in low cloud albedo as in SP-CAM.

1. Introduction

The uncertain response of clouds to climate change remains a central focus of many research efforts. Understanding low-cloud changes is a particular priority because of the large influence of low clouds on the global albedo. A superparameterized climate model is attractive for this purpose because it sidesteps the complex suite of moist physics parameterizations that control simulated boundary-layer cloud in conventional general circulation models (GCMs). Instead, the cloud-topped bound-

ary layer is explicitly simulated with a two-dimensional coarse-resolution cloud-resolving model. This approach has its own limitations but they are somewhat complementary to those of conventional GCMs. Hence results from a superparameterized GCM are interesting to understand and compare with conventional GCMs. Since the computational expense of a superparameterized GCM is roughly 100-fold larger than for a conventional GCM with the same global grid resolution, it is sensible to start by focusing on climate changes that can

To whom correspondence should be addressed.

Matthew C. Wyant, Department of Atmospheric Sciences, University of Washington, Seattle, WA, 98195-1640, USA
e-mail: mwyant@atmos.washington.edu

analyzed using simulations of just a few years.

In past work, we have looked at the response of a superparameterized version of the Community Atmosphere Model (SP-CAM) to one such idealized climate perturbation. Wyant *et al.* (2006) compared a SP-CAM simulation with specified climatological sea-surface temperature (SST) distributions with a perturbation simulation in which SST was uniformly increased by 2K. They found that SP-CAM had a strong increase in marine low clouds in the warmer climate, indicating a negative climate feedback. These experiments were further explored in Wyant *et al.* (2009) (hereafter W09) by focusing on regions of strong lower tropospheric stability (LTS), where mid and deep convection is suppressed and low cloud is the dominant cloud type. The tropical low-cloud cover increase was attributed to increased radiative cooling and stronger capping inversions in the warmer climate. We analyzed these changes in Blossey *et al.* (2009) (hereafter B09) using multiple cloud-resolving model (CRM) experiments. Large-scale environmental forcing from SP-CAM composite output in high LTS regions was used to force the CRM. The CRM low-cloud response to the +2K SST perturbation was qualitatively similar to the SP-CAM response, though its amplitude was strongly dependent on the resolution of the CRM.

The ‘fast’ response of the climate system to CO₂ changes has been highlighted in many recent studies (e.g. Gregory and Webb (2008), Andrews and Forster (2008), Bala *et al.* (2009), Andrews *et al.* (2009), Cao *et al.* (2011), Colman and McAvaney (2011), and Lambert *et al.* (2011)). By ‘fast’ time scales we mean a few months or less, much shorter than the several-year timescale on which the SST responds to a CO₂ change. Gregory and Webb (2008) used GCMs coupled to a slab-ocean model. They demonstrated how the fast response to a large increase in CO₂ can be separated from the slow response of the climate as the oceanic surface mixed layer adjusts to the imposed perturbation and warms the atmosphere. They went on to show that the fast response also can be isolated by applying the CO₂ increase while keeping SSTs fixed. This type of experiment is far more computationally feasible for SP-CAM than a slab-ocean experiment, the latter of which would require a ~ 25 -year spin up of the atmosphere/ocean system. Other previous studies mainly focused on the fast response of different aspects of the global-mean hydrological cycle and clouds, noting a reduction in precipitation associated with weaker atmospheric radiative cooling (Bala *et al.* 2009; Andrews *et al.* 2009; Cao *et al.* 2011), and a

reduction in cloud cover in most models (Andrews and Forster 2008).

In this paper, we analyze an SP-CAM simulation of the fast cloud and circulation response to a quadrupling of CO₂ from present-day values while holding SST constant. In addition to use of SP-CAM, our study differs from past work by emphasizing shifts in low-latitude cloud, shifts in circulations between ocean and land, and simulated changes to the marine cloud-topped boundary layer. In Section 2 we describe the SP-CAM model. The 4xCO₂ experiment design is presented in Section 3. In Section 4 we briefly describe how we correct SP-CAM cloud forcing calculations for cloud-masking effects. Section 5 describes the overall response of SP-CAM to the 4xCO₂ perturbation. The marine low cloud response is analyzed in Section 6 utilizing CRM experiments. In Section 7 we further discuss the results and conclude.

2. Model Description

SP-CAM, as described in Khairoutdinov *et al.* (2005) consists of the Community Atmospheric Model (CAM, Collins *et al.* 2006) run with a two-dimensional CRM embedded in each model grid column. The System for Atmospheric Modeling (SAM, Khairoutdinov and Randall, 2003) is used as the embedded model.

The versions of SP-CAM used in this study are very similar, though not identical, to those used in W09 and B09. The version of SAM used here in the single column CRM simulations in section 6 are identical to those in B09. CAM 3.1 is run using a semi-Lagrangian dynamical core, 30 vertical levels, and 2.8 degree x 2.8 degree horizontal grid spacing. In each grid column of SP-CAM, SAM is run with 32 grid columns 4km apart, oriented in the north-south direction. Each SAM domain replaces moist convective parameterization and cloud processes in that grid-column of CAM. More model details can be found in W09 and Wyant *et al.* (2006).

To analyze the low-cloud response, we also use SAM run offline from SP-CAM. The setup for SAM for these experiments is described below.

3. Experiment Setup

Both control and 4xCO₂ experiments are performed with fixed present-day climatological SST and sea-ice adopted from the UK Met Office Hadley Center’s HadISST1 dataset (Rayner *et al.* 2003). Both control

and 4xCO₂ simulations are run for 2.5 years with the first 1/2 year spin up discarded from our analysis. A monthly climatology for 30N to 30S is produced by averaging each month's output over two simulation years. A longer simulation pair would have been preferable for better averaging across the natural variability of clouds, but the 4xCO₂ radiative perturbation is strong enough to induce a clearly detectable response even in the two-year period which we compare.

4. Correcting Cloud Forcing

We define the net top-of-atmosphere (TOA) cloud forcings using the typical sign conventions: (positive) longwave cloud forcing, $LWCF = LW_{clear} - LW$ and (negative) shortwave cloud forcing $SWCF = SW - SW_{clear}$ where LW is the net upward longwave TOA flux, SW is net downward shortwave TOA flux, and LW_{clear} and SW_{clear} are corresponding clear-sky fluxes.

Cloud radiative forcings, while illuminating, have cloud-masking biases that must be removed before they are good measures of the radiative effect of cloud changes on climate (Soden et al. 2004). These biases occur for our case because the same cloud will have a slightly different cloud radiative forcing if CO₂ is instantaneously quadrupled. The cloud-masking correction would ideally be estimated using side-by-side radiative transfer calculations from the control simulation with control and perturbed CO₂, but these are not available for this simulation. Because the cloud-masking depends only on the control cloud distribution and not the cloud changes, it can be expected to be similar between GCMs that have a fairly realistic cloud climatology. Thus, we estimate the cloud-masking contribution to LWCF and SWCF for SP-CAM from side-by-side radiation calculations with control and quadrupled CO₂ made for a control-climate simulation of a different GCM, the United Kingdom Met Office (UKMO) HadGEM2 GCM with fixed SST.

Figure 1 shows maps of the annual-mean HadGEM2 LWCF and SWCF response to 4xCO₂ with clouds unchanged. Clouds cause positive LWCF by intercepting outgoing longwave radiation - as CO₂ is quadrupled and outgoing longwave radiation is reduced, this effect is reduced. In HadGEM2 instantaneously increasing CO₂ reduces LWCF by a little more than 1 W m⁻² in both the global and tropical mean. This negative cloud-masking contribution to LWCF is largest in regions of extensive high clouds. The much smaller cloud-masking contri-

bution to SWCF occurs mainly over regions of extensive low cloud (Fig. 1b) where SWCF is strongly negative. The intensity of the light reflected by these clouds that reaches the top of the atmosphere is reduced slightly by CO₂ absorption, reducing the magnitude of SWCF. Therefore in low-cloud regions, an atmosphere with increasing CO₂ tends to make SWCF less negative. This small effect is even smaller in the case of optically thick high cloud, because of the shorter optical path (and therefore absorption by CO₂) from the top of the cloud to the top of the atmosphere. The global mean increase in SWCF due to cloud masking is only 0.12 W m⁻².

We apply the HadGEM2 cloud masking to the response of SP-CAM LWCF and SWCF subsequently shown in Figures 2 and 10 and Tables 1 and 2.

5. The SP-CAM Fast 4xCO₂ Response

5.1. The Global Response

We begin with brief summary of the fast global response of SP-CAM to CO₂ quadrupling. We will then focus on the tropical response for the remainder of the paper.

The global and tropical mean (30S-30N) values for the control run and their changes with 4xCO₂ are shown in Table 1. The radiative impact of the 4xCO₂ perturbation is dominated by shift of effective emission to space of longwave radiation to colder temperatures, reducing the net emission. At the top of the atmosphere, net outgoing longwave radiation is reduced by 6.7 W m⁻² and the clear-sky net outgoing longwave is reduced by 8.0 W m⁻², while net incoming all-sky and clear-sky shortwave radiation increases only 0.1 W m⁻² and 0.2 W m⁻², respectively. The reduction of clear-sky TOA net longwave radiation is about 8% larger in SP-CAM than the estimated model-ensemble mean value in the 4xCO₂ experiments of Gregory and Webb (2008).

There is a significant slowing of the hydrological cycle with global-mean reduction in precipitation and surface latent heat flux. The fast impact of increased CO₂ on the global hydrological cycle has been the focus of many recent modeling studies (e.g. Bala et al. (2009), Andrews et al. (2009), Wu et al. (2010), Andrews and Forster (2010), Cao et al. (2011)). SP-CAM's 4% reduction in precipitation is similar to the precipitation reduction of 3.6% in the Community Atmosphere Model (CAM) 3.1 reported in Bala et al. (2009) (based on doubling the response of their 2xCO₂ experiment). It is substantially less than the 7% global precipitation reduction in the UK Met office Hadley Center model (HadCM3L) reported in

Cao *et al.* (2011).

There is a slight increase in total cloud fraction (0.5%) led by modest increases in high and low clouds, and partially offset by a loss of middle clouds. The global mean total condensed water in the troposphere changes only slightly; the small 0.2 g m^{-2} increase in liquid water path (LWP) is offset by a 0.2 g m^{-2} decrease of ice water path (IWP).

Global maps of mean change of LWCF and SWCF are shown in Figure 2, corrected by cloud mask (LWCF and SWCF of the control simulation are very similar to those presented in an earlier version of SP-CAM shown in Khairoutdinov *et al.* (2005)). There are very large regional changes in LWCF and SWCF, especially in the tropics due to local cloud changes. However the corrected global mean changes of LWCF and SWCF are each only about -0.2 W m^{-2} .

Tropical-mean changes in Table 1 are qualitatively similar to global-mean changes in most regards - cloud cover changes only slightly and the strength of the hydrological cycle is reduced. For the remainder of the paper we shift our focus to tropical changes.

5.2. Tropical-mean $4\times\text{CO}_2$ changes in radiation and precipitation

Here we analyze the response of salient cloud-related variables in both tropical-mean (30S-30N), and partitioned between tropical land and ocean. Since both land and ocean encompass a wide variety of dynamical regimes, we use similar methodology to Bony *et al.* (2004) to sort tropical column-months (land, ocean, or both) using monthly-mean pressure velocity at 500 hPa, ω_{500} , and examine the responses in this dynamically binned framework.

Table 1 includes statistics computed separately over tropical land and ocean regions. As tropical land coverage is only about 25%, the overall statistics are heavily influenced by the ocean regions. However the mean changes over land due to $4\times\text{CO}_2$ are stronger and almost always of opposite sign to the changes over ocean, so the changes over land regions prove to also be important to the tropical mean. Colman and McAvaney (2011) also discuss some opposing fast responses over ocean and land in their experiments.

The overall net outgoing longwave (LW) flux at the top of the tropical atmosphere is reduced by 8.0 W m^{-2} (Table 1) due to a higher and colder effective CO_2 emission level. There is also reduced LW surface cooling

over both tropical ocean and land, but this mean reduction is smaller (3.3 W m^{-2}). Therefore the atmospheric column-integrated LW cooling is reduced by 4.7 W m^{-2} . There are much smaller increases in net downward SW fluxes at the TOA (0.4 W m^{-2}) and at the surface (0.1 W m^{-2}) which slightly further reduce the net tropospheric radiative cooling.

Radiative cooling is present throughout the troposphere, but it is particularly strong (1.7 K day^{-1}) near the top of the boundary layer between 800 and 900 hPa due to the strong vertical gradient of water vapor mixing ratio. With the increase of CO_2 , radiative cooling is reduced by $0.1\text{-}0.2 \text{ K day}^{-1}$ in most of the lower troposphere, especially at the top of the boundary layer (Figure 3, magenta dashed line). We also performed off-line calculations of the clear-sky radiative heating rates using the mean ω -sorted and averaged temperature and moisture profiles. These are averaged over all ω 's and also plotted in Fig. 3 (light blue dot-dashed line). Above 900 hPa, the clear-sky changes are similar to the full model radiative cooling changes. This implies that the decrease in lower to mid-tropospheric radiative cooling is primarily a clear-sky phenomenon, and not mainly a result of fast cloud changes. In the layer near the surface (900-1000 hPa) the reduction of SP-CAM radiative cooling is much weaker than predicted from the clear-sky change, presumably due to the effects of boundary layer cloud.

Accompanying the reduction in tropospheric radiative cooling is a reduction in tropical-mean precipitation by 0.13 mm day^{-1} (Table 1), or 3.8%, and a reduction in condensational heating of 3.8 W m^{-2} . The surface latent heat flux is similarly reduced by 3.9 W m^{-2} .

The precipitation and its change can usefully be analyzed using dynamical ω_{500} -binning. Figure 4a shows the expected strong linear relationship between precipitation and ω in ascent regions over both land and oceans, with strongest precipitation in regions of strongest mid-tropospheric ascent. With the quadrupling of CO_2 precipitation is reduced across almost all tropical ω regimes (Fig. 4b), especially in most regions of strong ascent.

There is also a positive 'dynamic' contribution to the precipitation response (in the terminology of Bony *et al.* (2004)) due to a slight shift in the tropics-wide ω PDF toward more mean ascent (see next section), but it has only about 15% of the amplitude of the sum of the 'thermodynamic' contribution plotted here.

5.3. Shifts Between Ocean and Land

One key feature of the perturbed climate is the change in land surface temperature, as shown in Figure 5. Over most of the globe, the land-surface temperature increases with a global land-mean increase of 0.87K. An ensemble average of 10 climate models in Andrews et al. (2009) gives a fast global land surface warming of 0.49 K for a 2xCO₂ perturbation, so the SP-CAM land warming response is a little weaker than most of these models. The tropical-mean land temperature increase is SP-CAM is 0.50 K, with especially strong surface warming in tropical deserts. The land temperature increase is primarily caused by the greenhouse effect of the added CO₂. That is, even before any change in atmospheric temperature or moisture, the downward flux of infrared radiation increases. The land surface temperature warms rapidly because of its weak thermal inertia until a new radiative balance is reached. This surface warming is reduced by the tropospheric export of moist static energy from land columns to ocean columns (see Lambert et al. 2011). Additional mechanisms for land-sea surface temperature contrast in both transient and equilibrium climate perturbation experiments are considered in Joshi et al. (2008), Dong et al. (2009), and Lambert et al. (2011).

With increased CO₂ in SP-CAM, there is a general tropospheric warming, particularly over land (Fig. 6), where it increases with height reaching a maximum in the upper troposphere at about 280 hPa. Over the ocean, the warming profile also has a second maximum at 820 hPa discussed further in Section 5.4.

A consequence of the warming of land surfaces relative to fixed SSTs and relatively stronger tropospheric warming over land is a shift of convection from ocean to land regions. There is an increase of mean ascent in the mid-troposphere ($-\omega_{500}$) over land by almost 3 hPa day⁻¹, and the fraction of overall tropical precipitation that falls over land areas increases 18%. The shift to land is further examined in Figure 7 which shows PDFs of ω_{500} for the control climate and their changes with increased CO₂. Here the column-months are sorted into bins of 20 hPa day⁻¹ from -190 hPa day⁻¹ to 150 hPa day⁻¹. This sorting is done separately for land regions (red dashed line), ocean regions (blue dash-dotted line), and the entire tropics (black solid line). In the control climate (Fig. 7a), the ω_{500} PDFs for ocean and land are fairly similar. The dominant feature of the changes over land (Fig. 7b) is a shift in PDF from regions of mean subsidence to those where mean upward motion is already strong (from -50 to -130 hPa day⁻¹). The PDF changes

over ocean regions are generally the opposite in sign but much weaker. The overall response of the tropics-wide PDF is a slight shift away from extreme values of ω_{500} (slowdown of the overturning circulation) and also a slight shift toward mean ascent. A similar shift in circulation is also noted in HadAM3 2xCO₂ experiments in Lambert et al. (2011).

Figure 8 shows a conceptual diagram of these changes. Increasing downward longwave radiation leads to warmer land surface temperatures and a larger land-ocean thermal contrast (due to the fixed SSTs). This in turn leads to more upward motion and convection, more clouds at all vertical levels, and more precipitation over land with opposite effects over the oceans. While the fixed SSTs in the 4xCO₂ experiment are somewhat unrealistic, even in a coupled ocean-atmosphere GCM the larger thermal inertia of the ocean relative to land would lead to much slower warming of the ocean surface than the land surface and a larger land-ocean thermal contrast. As a result, the changes seen here would likely be present in the early years of experiments with instantaneous increases of CO₂ in coupled models.

We now examine some elements of this conceptual picture in more detail, beginning with land-ocean shifts in precipitation due to increasing CO₂. Land precipitation increases strongly (+0.25 mm day⁻¹) and ocean precipitation decreases strongly (-0.25 mm day⁻¹) (Table 1) associated with the shift of strong ascent and deep convection from ocean to land regions.

The 4xCO₂ liquid water path (LWP) and ice water path (IWP) respond to this shift of convection, increasing sharply over land and decreasing more modestly over ocean (Table 1). These effects largely cancel in the tropical mean. The tropical mean LWP is reduced by only about 1.2 g m⁻² or 1.6% and the tropical mean IWP increases by only 0.1 g m⁻² or 0.6%.

The combined land and ocean cloud fraction sorted by ω are presented in Figure 9. Henceforth in the paper we follow W09 and use percentile binning. The advantage of this method is that each bin represents an equal surface area, so an unweighted average across bins gives the tropical mean. Since the omega values at the bin-boundaries are free to shift when using percentile-binning, changes of bin-mean quantities represent a combination of dynamic and thermodynamic contributions computed when using specified ω -valued bins. For most variables of interest in this study, the thermodynamic contributions (in this case, cloud profile changes at constant ω) are dominant (not shown).

The control cloud fraction (Fig 9a) is dominated by high clouds in the strongest ascent regions where precipitation is strongest. In the lower troposphere, vertical profiles of low cloud peak at around the 900 hPa level, with peak single-level cloud fractions > 0.1 in regions of moderate to strong subsidence. The changes in cloud fraction (Fig 9b) indicate a general increase (and perhaps a slight lifting) of high clouds in the ascent regions associated with the IWP increase. Cloud fractions in the lower troposphere are reduced tropics-wide from 800 to 900 hPa, but this is compensated by an increase in cloud fraction nearer to the surface, particularly in moderate to strong subsidence regions. In these subsidence regions, the vertical dipole pattern of decreasing cloud fraction near cloud top and increasing cloud fraction below is suggestive of a shallowing of the boundary layer and will be further explored in Section 5.4.

The tropics-wide ocean and land changes in cloud fraction at various tropospheric levels (Table 1) mirror the circulation changes and largely cancel in tropical-mean. Over ocean, there is a weak mean decrease in cloudiness at all levels, while over land cloudiness increases at all levels, with an especially strong 0.02 increase in high clouds. The total tropical cloud cover increases only by about 0.002 or a relative increase of 0.4%.

The overall radiative impact of these cloud changes is similarly small. Figure 10a presents ω_{500} percentile-binned tropical-mean simulated LWCF and SWCF for the control simulation. At all percentiles, the shortwave cooling effect of clouds is larger than the longwave heating effect. The amplitudes of both LWCF and SWCF increase to the left, towards increasing deep convection and associated high and middle clouds. Net cloud forcing in subsiding regions, where high cloud is minimal, is controlled by low clouds, which cause negative SWCF by reflecting shortwave radiation, and only slightly influence LWCF.

The respective changes to SWCF and LWCF (Fig 10b) due to $4\times\text{CO}_2$ are generally weakly positive and negative, with tropical mean changes of $+0.3 \text{ W m}^{-2}$ and -1.2 W m^{-2} (Table 1) (A similar weak cloud forcing response is seen in the HadAM3 GCM experiments of Lambert *et al.* (2011)). When corrected by cloud masking, the tropical changes are only 0.2 W m^{-2} and -0.1 W m^{-2} , respectively.

Hence the inferred SP-CAM $4\times\text{CO}_2$ tropical-mean longwave and shortwave cloud radiative feedbacks are both very small, consistent with the very small simu-

lated tropical-mean cloud cover changes and the cancellation of compensating longwave effects of slight boundary layer cloud height decreases and tropopause cirrus cloud height increases.

5.4. Marine Low Cloud Response

In discussing Fig. 9, we noted a change in the vertical profile of cloud fraction suggestive of a tropical-mean lowering of boundary-layer cloud. In low latitudes, boundary-layer clouds are concentrated over the cooler parts of the oceans. As the final part of this study, we analyze why CO_2 quadrupling might lead to an overall lowering of MBL cloud heights in these regions. We argue for two possible mechanisms. One is the enhancement of downwelling longwave radiation in the free troposphere with increased CO_2 . This results in less radiative destabilization of marine cloud-topped boundary layers, lower turbulent entrainment, and hence a shallower boundary layer top. This mechanism was introduced in Caldwell and Bretherton's (2009) mixed-layer-model study of subtropical stratocumulus response to climate change. The second mechanism is a general warming of the low-latitude lower troposphere due to reduced longwave cooling. In combination with fixed SST, this causes a strengthening of the trade inversion and thereby also inhibits turbulent entrainment.

To test the links implied in this argument, we start by analyzing SP-CAM monthly climatology in grid columns over ocean regions between 30S and 30N. We bin column-months using the lower tropospheric stability (LTS), defined here as the difference between potential temperature at 700 hPa and the SST. LTS is a skillful predictor of climatological marine low cloud amount (Klein and Hartmann, 1993) that differentiates marine low cloud regimes more effectively than ω_{500} . Within 30S-30N, LTS depends mainly on SST, with low LTS corresponding to high SST and vice versa. LTS-sorted ω and cloud fraction for the SP-CAM control and perturbation cases are shown in Figure 11. In the control case, we see as expected that in higher LTS regions, there is stronger tropospheric subsidence, more low cloud with a slightly lower typical altitude, and less high cloud. Because of the strong association of LTS with subsidence, it is not surprising that the general shape of the control cloud fraction distribution (Fig 11b) is similar to the tropics-wide ω -sorted distribution shown in Fig 9 (note different color scale).

In response to the CO_2 perturbation, the tropospheric

radiative cooling rate decreases (Fig. 3) so mean subsidence over the cooler oceans, which is predominantly radiatively driven, is also weakened (Fig 11c) (In these regions fast changes in tropospheric lapse rate and their impact on subsidence warming are small). For the top 50% of LTS column-months, a vertical dipole in MBL cloud change is apparent (Fig 11d) similar to the dipole seen in Fig. 9b. That is, the mean height of MBL cloud is lowered, though the vertically integrated change in marine low cloud fraction is slight. It is hard to precisely estimate the boundary layer depth reduction from the cloud profile change, but the height of the 50% relative humidity level, a proxy for the boundary layer capping inversion, drops about 80 m averaged across these LTS percentiles.

Another important change is the warming of the lower troposphere above the MBL also possibly caused by the CO_2 -induced reduction in radiative cooling. Fig. 6 (green dotted line) shows the LTS80-90 composite change in potential temperature, which has a maximum of about 0.6 K at 800 hPa. One significant contributor to this is just the lowering of the trade inversion itself. However, even at 600-700hPa, well above the mean inversion height, temperature increases much more than near-surface temperature, which is tightly coupled to the fixed SST. This suggests that the trade inversion not only lowers but also strengthens by 0.3-0.5 K.

6. Column simulations of $4xCO_2$ marine low cloud change

6.1. CRM Experiment Setup

To further investigate the boundary-layer height decrease in a more controlled modeling framework, we use the approach of B09 and try to replicate the SP-CAM cloud response using its native CRM model, SAM. We force SAM with bin-mean environmental conditions from SP-CAM averaged across the column-months comprising the 80th-90th percentile of LTS. We simulate the 80th-90th percentile in particular because it represents a regime of substantial low cloud cover with relatively little synoptic disturbance in the troposphere, so that steady-state MBL simulations can provide a reasonable analog to the mean SP-CAM state.

We use two contrasting resolutions in SAM (as in B09). The first, CRM4km, matches the SP-CAM sub-column CRM simulations. The horizontal resolution is 4km and the vertical resolution varies from ~ 130 m at the surface increasing to ~ 1 km at a height of 4km. The

domain extends 128km in the horizontal and 40km in the vertical. The second case, LES100, has 100m horizontal resolution and 40m vertical resolution in the lower troposphere. It is designed to more fully resolve the turbulent motions in the boundary layer and thereby assess the robustness of physical mechanisms seen in the coarse-resolution modeling frameworks. This case has a two-dimensional horizontally-periodic domain 51.2 km wide by 27 km deep. In both cases the CRM domain is oriented north-south as in SP-CAM.

We follow the procedure described in B09 for initializing and forcing the CRM experiments. In summary, the CRM experiments are initialized with bin-mean SST and profiles of temperature and specific humidity from the SP-CAM averaged over the 80-90th LTS percentile. The vertical profiles of horizontal wind are nudged to match the mean wind speed from SP-CAM. Above the MBL, specific humidity is nudged back to SP-CAM values. LTS-bin-mean large-scale advective tendencies of heat and moisture from SP-CAM are imposed uniformly on the entire CRM domain and are nearly identical to those shown in B09. A separate set of forcings is computed from each of the control and $4xCO_2$ SP-CAM experiments and applied to create a control and $4xCO_2$ CRM simulation pair.

The binned vertical velocity profile from SP-CAM is used for the CRM runs, but is adaptively modified using the weak-temperature-gradient approach of B09. This approach slowly adjusts the evolving CRM temperature profiles towards SP-CAM values through small changes in the subsidence profile. The SP-CAM ω profile and the profiles that develop in each CRM control experiment are shown in Figure 12a. There is mid-tropospheric subsidence of about 25-30 hPa day^{-1} decreasing below the mean MBL top near 900 hPa. The differences in imposed ω between the $4xCO_2$ and the control are shown in Figure 12b. The subsidence in the perturbed case is reduced by 4-8% in the boundary layer and lower free troposphere, both in SP-CAM and the modified profiles, due to the reduced radiative cooling. The subsidence reduction in the lower free troposphere in SP-CAM is about twice as large as that seen in the +2K SST SP-CAM experiments of B09. In contrast to the $4xCO_2$ response here, in the boundary layer in high LTS regions, subsidence strengthens slightly with +2K SST in the W09 experiment (compare Fig. 11c with W09 Fig. 4f).

Differences between the $\Delta\omega$ profiles of the CRM4km and LES100 cases and SP-CAM in Figure 12b are entirely the result of the ω adjustment to the virtual temper-

ature differences between the small-scale models and SP-CAM. In the free troposphere, these differences appear to be due to the presence of an anomalous 1K cold bias in the upper troposphere of the CRM4km and LES100 runs. The ω adjustment to this bias is nonlocal and reaches into the lower free-troposphere. The cold bias may be caused by the absence of infrequent deep convection or by the absence of the radiative effects of intermediate and high clouds. In the lower troposphere, the profile LES100 $\Delta\omega$ is more sharply negatively peaked due to adjustments to better-resolved temperature changes near the cloud-top. The smaller amplitude of $\Delta\omega$ in the cloud layer of the in the CRM4km case is the result of about 0.2 K less cloud-layer warming from $4xCO_2$ than occurs in SP-CAM (see below).

The CRM experiments are run to approximate steady state with diurnal radiative forcing. The CRM4km and LES100 runs extend for 1000 days and 100 days, respectively. Run mean statistics are computed starting at day 50 for both runs. The long averaging period for the CRM4km runs is used to reduce the noise due to internal temporal variability. The CRM4km and LES100 convergence to a steady state is very similar to that reported in B09.

6.2. CRM cloud and radiation changes

We compare vertical profiles of the CRM4km and LES100 steady states with the SP-CAM composites in Figure 13. For each variable the control profile is shown on the left and the change with $4xCO_2$ is shown on the right. The CRM4km and LES100 models produce steady state MBLs with many of the features of the SP-CAM composite. The SP-CAM potential temperature and relative humidity inversions are more smoothed out due to compositing. The SP-CAM cloud fraction matches fairly well to the CRM4km profile. The LES100 control simulation has significantly less cloud fraction and cloud liquid water though the primary vertical extent of cloud is similar to the other models. SP-CAM and CRM4km have a single vertical maximum of cloud fraction, while LES100 has two peaks corresponding to a cumulus layer below and a detraining stratus layer above. Despite these differences, the CRM4km and LES100 profile changes with $4xCO_2$ imply a shallowing of the MBL comparable to that in the SP-CAM composite, and hence are useful for better understanding the shallowing mechanism and its consequences for the cloud-topped boundary layer.

Table 2 compares some statistics of the CRM4km

and LES100 runs with the SP-CAM LTS80-90 composite. The tabulated inversion height, z_i , is estimated as the lowest height above the surface where the relative humidity drops to 50%. This value, together with the mean ω profile is also used to estimate the MBL entrainment rate, assuming steady state. The mean drop in inversion height in the CRM4km (63 m) and LES100 (114 m) runs brackets the SP-CAM composite (84 m).

The cloud statistics in Table 2 recap findings from the profile analysis above. The CRM4km control run approximates the SP-CAM composite fairly well in cloud fraction but has about 40% higher LWP. The higher resolution LES100 run produces has only about a fourth as much cloud fraction and LWP as SP-CAM, as in W09. As in Table 1, this LWP statistic includes clear grid cells/columns; the average LWP within cloudy grid columns is similar between LES100 and SP-CAM. In the SP-CAM LTS80-90 composite, there is negligible middle and high cloud fraction, and none in CRM4km and LES100.

The changes in the cloud-related statistics in Table 2 due to the $4xCO_2$ perturbation are not particularly strong. LWP decreases in SP-CAM by about 1.3 g m^{-2} (2%), but decreases by less than half as much in CRM4km. The LWP decrease of 1.0 g m^{-2} in LES100 is similar to SP-CAM in absolute terms but much larger relative to the control value. SP-CAM has almost no change in low cloud while the CRM4km has a 1% increase in low cloud (relative to control) and LES100 has a 2% decrease. Despite these diverse low cloud changes, the SWCF becomes slightly less negative in all three models. (Note the small HadGEM cloud-mask corrections have been applied to all values in parenthesis, with the CRM4km and LES100 corrections adjusted for cloud fraction.) For the CRM4km case, this change is unexpected because the cloud fraction increases and LWP only weakly decreases. Further analysis reveals the diurnal cycle of cloud cover in CRM4km is somewhat enhanced by $4xCO_2$, so that the *daytime* cloud-fraction and LWP (which are what matters for SWCF) are both reduced significantly.

The changes in potential temperature and relative humidity in the LES100 case are locally much larger than those in SP-CAM and the CRM4km case due to the presence of a stationary sharp inversion. Both the SP-CAM and CRM4km cases have a 0.5K warming and a 3-4% decrease in relative humidity peaking near the inversion level. The decrease in relative humidity is due to both increasing temperature and decreasing spe-

cific humidity (not shown). The temperature and relative humidity changes in SP-CAM and CRM-4km are similar to the fast subtropical zonal mean changes due to 4xCO₂ shown by Colman and McAvaney (2011) using the Center for Australian Weather and Climate Research Model (CAWCR) GCM. Colman and McAvaney (2011) show a global mean decrease in relative humidity in the lower troposphere with a peak reduction of about 2% centered at about 750 hPa and attribute part of this decrease to the temperature increase in the lower troposphere. Our results suggest that the lowering of the tropical/sub-tropical MBL inversion may be a significant part of the relative humidity reduction in these regions.

6.3. CRM analysis of CO₂-driven boundary layer shallowing mechanism

In this section, CRM simulations are used to examine the links in our hypothesized mechanisms of CO₂-driven boundary layer shallowing. In particular, we look for changes in downwelling longwave radiation, boundary-layer cooling, turbulence intensity, entrainment rate, and vertical temperature profiles induced by increased CO₂ levels.

The subtropical lower troposphere in SP-CAM LTS80-90 and both CRM analog simulations have similar 4xCO₂ longwave radiation changes. The downwelling longwave radiation increases about 9.6 W m⁻² at a reference level of 2.5 km above the MBL (Table 2) but less than 4 W m⁻² at the surface, as shown for the CRM simulations in Fig 14. The upwelling longwave flux profile changes much less because of the fixed SST. The result is a 5-6 W m⁻² reduction in the net MBL radiative cooling (Table 2), concentrated in the upper part of the boundary layer.

It might be imagined that this decreased radiative destabilization would reduce MBL turbulence, which correspondingly reduces the entrainment rate. Indeed, in both CRM4km and LES100 runs, the entrainment rate is lowered by 4-8%, comparable to SP-CAM (Table 2). Fig 15 shows profiles of a measure of turbulence intensity, the vertical velocity variance $\overline{w'^2}$, for CRM4km and LES100. For CRM4km, $\overline{w'^2}$ is slightly reduced throughout the boundary layer as expected, consistent with the MBL-top entrainment rate. However, in LES100, $\overline{w'^2}$ is reduced in the sub-cloud layer, but in the upper boundary layer, where $\overline{w'^2}$ is much more relevant to entrainment, its profile shifts downwards with little change in peak amplitude (The control $\overline{w'^2}$ is much

smaller in CRM4km, which under-resolves the dominant energy-containing eddies, than in LES100. Some consequences of this issue are discussed in B09). A heat budget analysis (not shown) shows that in the cloud layer, the reduction in radiative destabilization is counterbalanced by reduced precipitation heating in the shallower 4xCO₂ cloud layer, so that the net buoyancy production of turbulence is nearly unchanged.

Hypothetically, in a shallower stratocumulus-topped mixed layer in which cloud cover is larger and precipitation is less important, we anticipate the reduction of radiative cooling with 4xCO₂ would be larger. This reduction could not be balanced by latent heating, so there would be a more pronounced decrease in cloud-layer turbulence.

However, in the case at hand, we must find another factor that can reduce the entrainment rate and hence the MBL depth in LES100. Figure 13a shows that the lower troposphere warms about 0.5 K above the MBL, but only one-third as much near the surface. This roughly 8% strengthening of the trade inversion is a plausible explanation for the 8% entrainment reduction in LES100 case.

The study of Watanabe et al. (2011) suggests that reduced surface fluxes of sensible and latent heat play a central role in the reduction of boundary layer depth with increased CO₂. However, for the LTS80-90 bin in SP-CAM and our CRM experiments, the reductions in surface sensible and latent heat fluxes are small (< 1 W m⁻²) compared to other changes (Table 2). In neighboring LTS bins of SP-CAM, the reductions in latent heat flux with 4xCO₂ are larger, but large reductions in precipitation are mostly realized in low-LTS parts of the tropical oceans and therefore do not appear to significantly impact high-LTS boundary layer depth.

To summarize, the CRM4km control simulation is a useful analog to the SP-CAM for this marine tropical low-cloud regime and shows a possible mechanism of boundary-layer shallowing due to reduced radiative destabilization. The net marine low-cloud response to CO₂ quadrupling is small in both SP-CAM and CRM4km but suggests a slight reduction in daytime cloud albedo. As in B09, the higher resolution LES100 simulation has a significantly lower cloud fraction and LWP than CRM4km and SP-CAM. Nevertheless, it shows a comparable reduction in MBL depth to SP-CAM and also predicts a slight reduction in daytime cloud albedo.

7. Conclusions

This study examines the fast response of the tropical troposphere to an instantaneous quadrupling of CO₂ using the SP-CAM superparameterized atmospheric GCM. Fixed SSTs are used as a proxy to isolate the fast response to the CO₂ increase prior to any ocean warming.

One obvious response is a shift of tropical clouds and precipitation from ocean to land. This is due to land surface warming from increased downward longwave radiative flux and a thermally direct tropospheric response.

Consistent with other recent model studies, the global hydrological cycle is weakened by 4xCO₂ – there is a 3.8% reduction in tropical rainfall and a similar reduction in surface evaporation. The tropically averaged cloud cover changes and the cloud radiative feedbacks are weak compared to the +2K SST experiment with SP-CAM in B09. Note that the mean tropical equilibrium SST change in a coupled model with to 4xCO₂ would be expected (based on many other previous model studies) to be roughly 4K.

Another noteworthy SP-CAM response to CO₂ quadrupling is a shallowing of the subtropical MBL associated with reduced entrainment through the trade inversion. Using CRM and LES simulations of the response of a typical cloud-topped boundary layer region to the large-scale forcings associated with CO₂ quadrupling, we find two mechanisms this contribute to the entrainment reduction. The first is increased downwelling LW flux from the enhanced CO₂, which reduces MBL radiative cooling, and (in the CRM4km simulations) reduces turbulence. The second is a strengthened trade inversion driven by CO₂-driven warming of the free troposphere while the MBL temperature remains locked to the fixed SST.

A 4xCO₂ experiment with a large number of state-of-the-art GCMs is part of the ongoing Coupled Model Intercomparison Project Phase 5 (CMIP5). We expect the shallowing of the MBL and the tropical ocean-land shifts to be robust across GCMs while other aspects of the cloud changes may differ significantly from our simulations.

Many recent studies highlight the dependence of the atmospheric response on the nature of the climate perturbation (e.g. Gregory and Webb (2008), Bala *et al.* (2009), Andrews *et al.* (2009), Cao *et al.* (2011), Colman and McAvaney (2011)). In previous work with SP-CAM using an identical experimental framework (B09 and W09), we found that a +2K SST perturbation produced a tropospheric temperature rise generally greater

than 2 K, an increase in tropospheric radiative cooling and a strongly enhanced low cloud fraction due to enhanced MBL radiative cooling. That experiment also had a shift of tropospheric ascent in the tropics from land to ocean, opposite to the shift described here. Clearly the tropical cloud response depends heavily on the details of the imposed climate perturbation. Another corollary is that it is necessary to average over all cloud regimes over both land and ocean to isolate the overall cloud response; otherwise local dynamical changes may be the main driver of cloud changes. A more realistic SP-CAM simulation of climate change due to increasing CO₂ would combine elements of the response of both of our prior climate perturbation experiments.

As found in B09 the mean low-cloud structure in this study is highly dependent on the CRM resolution. This suggests that using better SP-CAM resolution is necessary to simulate low-cloud response in a more quantitatively realistic way. In particular, LES experience suggests that substantially increased vertical resolution will be required to credibly simulate cloud changes in stratocumulus regimes using a superparameterized climate model.

Acknowledgements: Many thanks to Mark Webb of the UK Met Office for providing HadGEM output and radiative calculations and for providing a helpful comments on this manuscript. Thanks also to the helpful comments of two anonymous reviewers. This work was supported by the Center for Multiscale Modeling of Atmospheric Processes (CMMAP) through NSF grant number ATM-0425247.

References

- Andrews, T., and P. M. Forster, 2008: CO₂ forcing induces semi-direct effects with consequences for climate feedback interpretations. *Geophys. Res. Lett.*, **35**, 1-5. L04802, doi:10.1029/2007GL032273.
- Andrews, T., P. M. Forster, and J. M. Gregory, 2009: A surface energy perspective on climate change. *J. Climate*, **22**, 2557-2570, doi: 10.1175/2008JCLI2759.1
- Andrews, T., and P. M. Forster, 2010: The transient response of global-mean precipitation to increasing carbon dioxide levels. *Environ. Res. Lett.*, **5**, doi:10.1088/1748-9326/5/2/025212
- Bala, G., K. Caldeira, and R. Nemani, 2009: Fast versus slow response in climate change: implications for the global hydrological cycle. *Clim. Dyn.*, doi: 10:1007/s00382-009-0583-y

- Blossey, P. N., C. S. Bretherton, and M. C. Wyant, 2009: Subtropical low cloud response to a warmer climate in a superparameterized climate model. Part II. Column modeling with a cloud resolving model. *J. Adv. Model. Earth Sys.*, **1**, Art #8, 14pp., doi: 10.3894/JAMES.2009.1.8.
- Bony, S., J. Dufresne, H. Le Treut, J. Morcrette, C. Senior, 2004: On dynamic and thermodynamic components of cloud changes. *Clim. Dyn.*, **22**, 71-86. doi: 10.1007/s00382-003-0369-6.
- Caldwell, P., and C. S. Bretherton, 2009: Response of a subtropical stratocumulus-capped mixed layer to climate and aerosol changes. *J. Climate*, **22**, 20-38. doi: 10.1175/2008JCLI1967.1
- Cao, L., G. Bala, and K. Caleira, 2011: Why is there a short-term increase in global precipitation in response to diminished CO₂ forcing? *Geophys. Res. Lett.*, **38**, L06703, doi:10.1029/2011GL046713.
- Collins, W. D., P. J. Rasch, B. A. Boville, J. J. Hack, J. R. McCaa, D. L. Williamson, B. P. Briegleb, C. M. Bitz, S.-J. Lin, and M. Zhang, 2006: The formulation and atmospheric simulation of the Community Atmospheric Model Version 3 (CAM3). *J. Climate*, **19**, 2144-2161, doi:10.1175/JCLI3760.1.
- Colman, R. A., and B. J. McAvaney, 2011: On tropospheric adjustment to forcing and climate feedbacks. *Clim. Dyn.*, doi: 10.1007/s00382-011-1067-4.
- Gregory, J., and M. Webb, 2008: Tropospheric adjustment induces a cloud component in CO₂ forcing. *J. Climate*, **21**, 58-71, doi: 10.1175/2007JCLI1834.1.
- Dong, B., J. M. Gregory, and R. T. Sutton, 2009: Understanding land-sea warming contrast in response to increasing greenhouse gases. Part I: transient adjustment. *J. Climate*, **22**, 3079-3097., doi:10.1175/2009JCLI2652.1.
- Joshi, M. M., J. M. Gregory, M. J. Webb, D. M. H. Sexton, and Tim C. Johns, 2008: Mechanisms for the land/sea warming contrast exhibited by simulations of climate change. *Clim. Dyn.*, doi: 10.1007/s00382-007-0306-1.
- Khairoutdinov, M. F., and D. A. Randall, 2003: Cloud resolving modeling of the ARM summer 1997 IOP: Model formulation, results, uncertainties, and sensitivities. *J. Atmos. Sci.*, **60**, 607-625, doi:10.1175/1520-0469(2003)060<0607:CRMOTA>2.0.CO;2.
- Khairoutdinov, M., D. Randall, and C. DeMott, 2005: Simulations of the atmospheric general circulation using a cloud-resolving model as a superparameterization of physical processes. *J. Atmos. Sci.*, **62**, 2136-2154, doi:10.1175/JAS3453.1.
- Klein, S. A., and D. Hartmann, 1993: The seasonal cycle of low stratiform clouds. *J. Climate*, **6**, 1587-1606.
- Lambert, H. F., M. J. Webb, and M. M. Joshi, 2011: The relationship between land-ocean surface temperature contrast and radiative forcing. *J. Climate*, **24**, 3239-3256.
- Rayner, N. A., Parker, D.E., Horton, E.B., Folland, C.K., Alexander, L.V., Rowell, D.P., Kent, and E.C., Kaplan, A., 2003: Global analyses of sea surface temperature, sea ice, and night marine air temperature since the late nineteenth century. *J. Geophys. Res.*, **108**, 29 PP. doi:10.1029/2002JD002670.
- Soden, B. J., A. J. Broccoli, and R. S. Hemler, 2004: On the use of cloud forcing to estimate cloud feedback. *J. Climate*, **17**, 3661-3665.
- Watanabe, M., H. Shiogama, M. Yoshimori, T. Ogura, T. Yokohata, H. Okamoto, S. Emori, and M. Kimoto, 2011: Fast and Slow timescales in the tropical low-cloud response to increasing CO₂ in two climate models. *Clim. Dynamics*, doi: 10.1007/s00382-011-1178-y
- Wu, P., R. Wood, J. Ridley, and J. Lowe, 2010: Temporary acceleration of the hydrological cycle in response to a CO₂ rampdown. *Geophys. Res. Lett.*, **37**, L12705, doi:10.1029/2010GL043730
- Wyant, M. C., M. Khairoutdinov, and C. S. Bretherton, 2006: Climate sensitivity and cloud response of a GCM with a superparameterization. *Geophys. Res. Lett.*, **33**, L06714, doi:10.1029/2005GL025464.
- Wyant, M. C., C. S. Bretherton, and P. N. Blossey, 2009: Subtropical low cloud response to a warmer climate in a superparameterized climate model. Part I. Regime sorting and physical mechanisms. *J. Adv. Model. Earth Sys.*, **1**, Art. #7, 11pp., doi:10.3894/JAMES.2009.1.7.

Table 1: Mean statistics for the SP-CAM control simulation and changes due to the $4\times\text{CO}_2$ perturbation. All tropical mean statistics are for 30N-30S. All radiative and surface fluxes have units of W m^{-2} . SWCF and LWCF changes in parenthesis are corrected for cloud-masking effects (see discussion in 5.3). (*Note: for ω_{500} , the percentage change is normalized with the tropical-mean absolute value of the control ω_{500} .)

	Control				$\Delta_{4\times\text{CO}_2}$				Trop. Total %
	Trop. Ocean	Trop. Land	Trop. Total	Global	Trop. Ocean	Trop. Land	Trop. Total	Global	
Surface Temperature	299.2	298.2	299.0	288.1	0.0	0.5	0.1	0.3	0.0
ω_{500} (hPa day^{-1})	0.93	-1.98	0.20	0.02	0.71	-2.98	-0.22	-0.00	* -0.8
Low Cloud Fraction	0.303	0.154	0.265	0.359	-0.0011	0.0056	0.0006	0.0014	0.2
Middle Cloud Fraction	0.060	0.095	0.069	0.149	-0.0032	0.0057	-0.0010	-0.0020	-1.4
High Cloud Fraction	0.173	0.168	0.172	0.165	-0.0042	0.0203	0.0020	0.0023	1.2
Total Cloud Fraction	0.433	0.310	0.402	0.487	-0.0038	0.0184	0.0018	0.0008	0.4
LWP (g m^{-2})	82.3	64.3	77.8	75.5	-2.9	3.9	-1.2	0.2	-1.6
IWP (g m^{-2})	24.7	25.5	24.9	29.1	-0.8	3.1	0.1	-0.2	0.6
Rainfall (mm day^{-1})	3.61	2.39	3.30	2.75	-0.25	0.25	-0.13	-0.11	-3.8
LH Flux	135.1	46.1	112.7	79.7	-5.8	1.5	-3.9	-3.1	-3.5
SH Flux	13.9	58.8	25.2	23.0	-1.0	0.0	-0.7	-0.7	-3.0
SWCF	-63.9	-44.3	-59.0	-55.3	1.3	-2.5	0.3 (0.2)	-0.1 (-0.2)	0.6 (0.4)
LWCF	30.8	28.1	30.1	27.7	-2.2	1.5	-1.2 (-0.2)	-1.4 (-0.2)	-4.1 (-0.5)
Net SW dn TOA Clr	359.0	321.0	349.5	287.2	-0.0	0.1	0.0	0.2	0.0
Net LW up TOA Clr	284.4	285.5	284.7	261.9	-9.2	-9.4	-9.2	-8.0	-3.2
Net SW dn TOA	295.1	276.8	290.5	231.9	1.3	-2.4	0.4	0.1	0.1
Net LW up TOA	253.6	257.4	254.6	234.2	-7.0	-10.9	-8.0	-6.7	-3.1
Net SW dn Surf.	205.2	185.1	200.1	156.2	1.2	-3.2	0.1	-0.2	0.1
Net LW up Surf.	53.5	81.8	60.6	54.6	-2.7	-5.3	-3.3	-3.1	-5.5

Table 2: Mean LTS80-90 control and 4xCO₂ perturbation statistics for SP-CAM and steady-state model simulations. MBL depth z_i is based on the height of 50% relative humidity. SWCF changes in parenthesis are corrected for cloud-masking effects. Downwelling LW fluxes are unavailable for the SP-CAM experiment.

	Control			Δ_{4xCO_2}		
	SP-CAM	CRM4km	LES100	SP-CAM	CRM4km	LES100
Low cloud fraction	0.370	0.359	0.098	0.000	0.005	-0.002
LWP (g m ⁻²)	67.1	93.1	18.3	-1.3	-0.6	-1.0
Precipitation (mm d ⁻¹)	0.60	0.41	0.23	-0.06	-0.07	-0.04
Latent heat flux (W m ⁻²)	126.3	124.7	123.3	-0.9	0.2	-0.7
Sensible heat flux (W m ⁻²)	12.9	8.8	9.2	-0.7	-0.7	-0.4
SWCF (W m ⁻²)	-57.8	-44.0	-12.2	0.6 (0.4)	1.5 (1.3)	0.6 (0.6)
Downwelling LW, 2.5km (W m ⁻²)	-	230.4	245.0	-	9.7	9.6
Net down rad. flux, 2.5km (W m ⁻²)	101.3	127.8	161.7	8.6	9.4	8.0
MBL rad. cooling (W m ⁻²)	57.2	67.0	32.7	-6.0	-5.3	-4.9
MBL entrainment rate (mm s ⁻¹)	3.39	3.69	3.30	-0.23	-0.15	-0.27
MBL depth z_i (m)	2120	2018	1712	-84	-63	-114

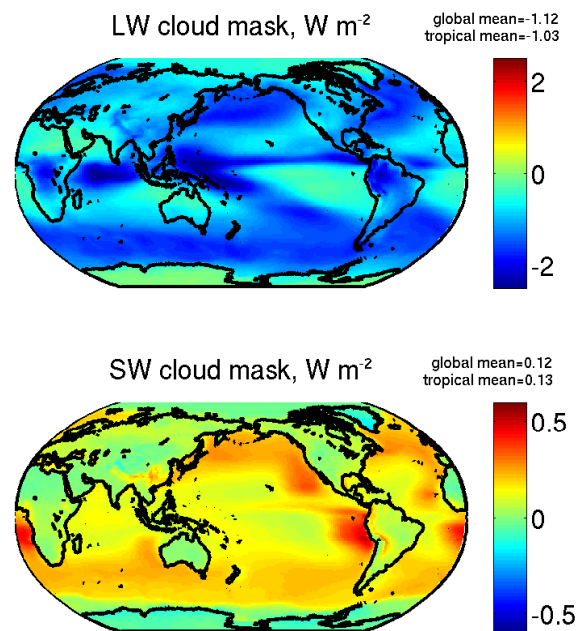


Figure 1: Change in calculated (a) LWCF and (b) SWCF in W m⁻² due to instantaneous 4xCO₂ for HadGEM2 climate model, based on offline radiation calculations with clouds and other atmospheric and surface properties held fixed. Data provided by Mark Webb of UKMO.

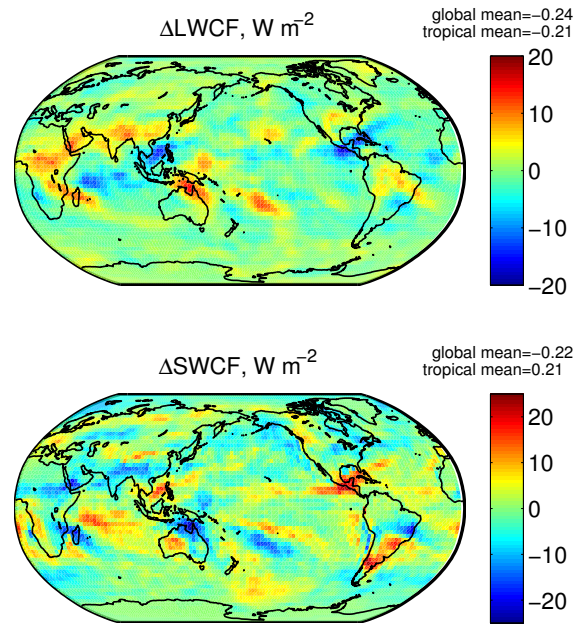


Figure 2: Change in SPCAM (a) LWCF and (b) SWCF in W m^{-2} due to instantaneous $4\times\text{CO}_2$. These values have been corrected using a cloud mask from the HadGEM climate model (see text).

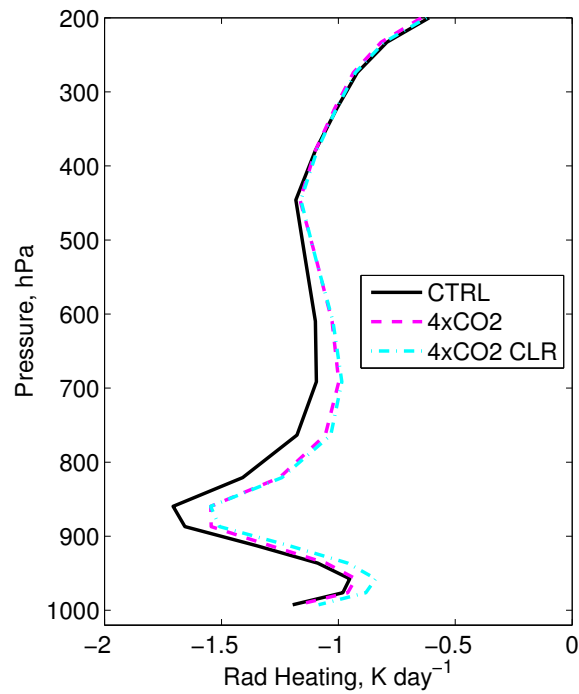


Figure 3: SP-CAM tropical mean heating rates in K day^{-1} for control (black solid), $4\times\text{CO}_2$ (magenta dashed), and control plus clear sky change due to $4\times\text{CO}_2$ (light blue dot-dashed, computed offline).

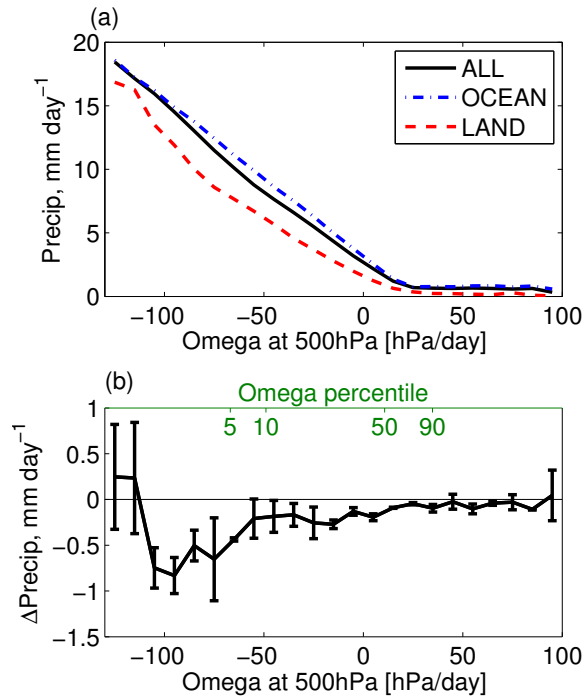


Figure 4: (a) Surface precipitation in mm day⁻¹ for ocean (blue dot-dashed) land (red dashed), and tropics-wide (black solid) sorted by ω_{500} . (b) Precipitation changes due to 4xCO₂ with error bars estimated from precipitation differences for simulation year 1 and year 2 considered separately. Omega percentiles are indicated in green at the top of the plot.

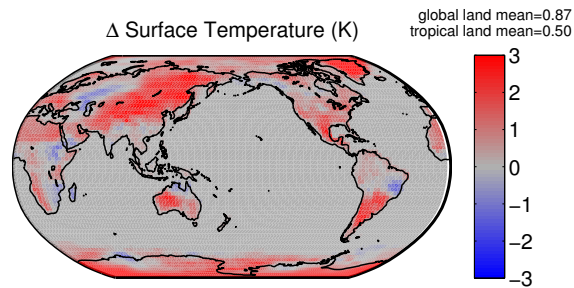


Figure 5: Annual mean change in surface temperature for SP-CAM due to 4xCO₂.

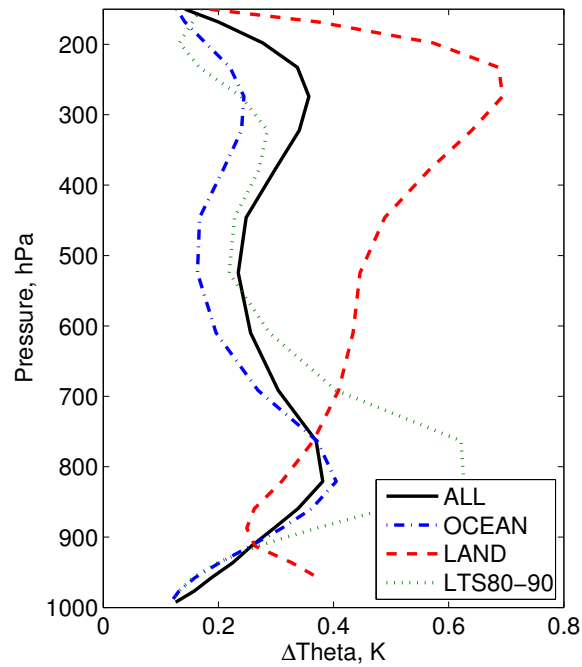


Figure 6: SP-CAM mean potential temperature change in K for all tropical columns (black solid), ocean (blue dash-dotted), land (red dashed), and regions with stable MBL's (green dotted) to be discussed in Section 5.4. Note that temperature changes at each pressure level are computed only for above-surface points, so the population of columns represented varies with pressure level near the surface. The land profile is plotted only to about 960hPa, the median tropical land surface pressure.

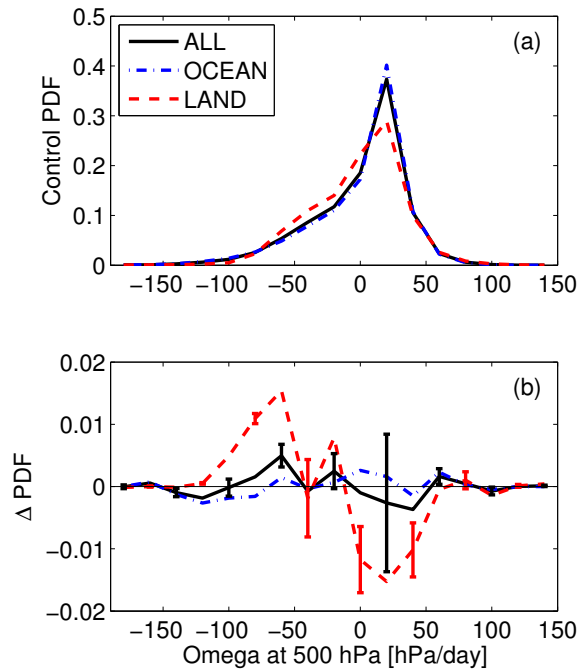


Figure 7: (a) PDF of tropical monthly pressure velocity ω at 500 hPa and (b) its change due to 4xCO₂, for SP-CAM. Separate PDF's are plotted for ocean (blue dash-dotted), land (red dashed) and all points (black solid). Error bars are estimated from PDF changes of years one and two considered separately.

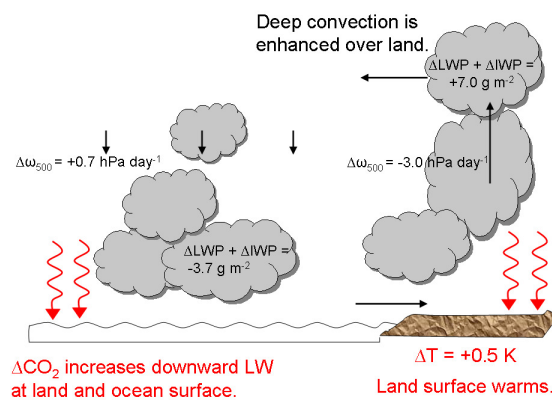


Figure 8: Conceptual picture of rapid tropical cloud changes due to increasing CO₂ shown together with mean tropical SP-CAM changes.

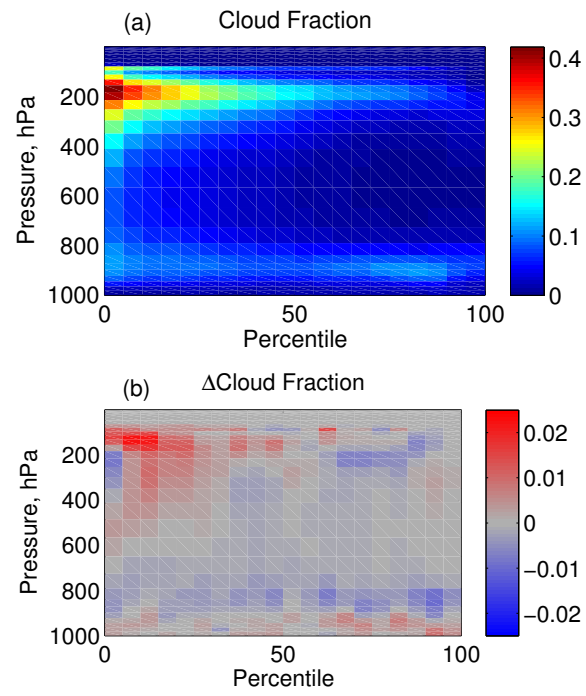


Figure 9: (a) ω -sorted cloud fraction and (b) the change due to the CO_2 perturbation.

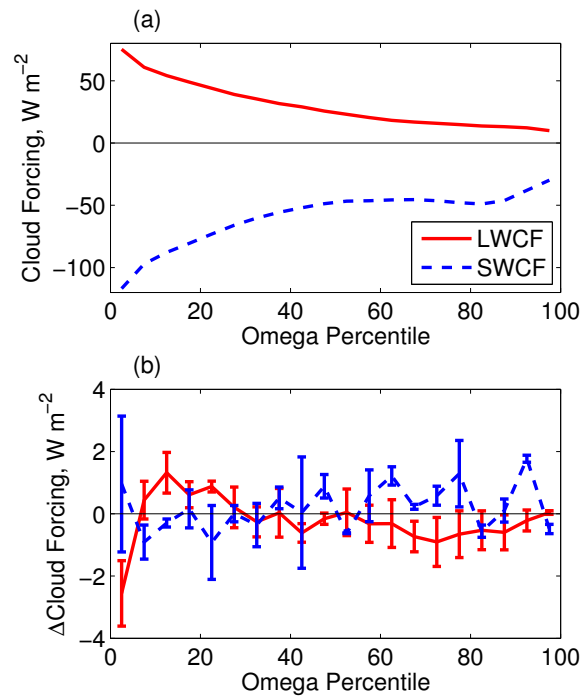


Figure 10: (a) SP-CAM ω sorted longwave (red solid) and shortwave (blue dashed) cloud forcing in W m^{-2} and (b) changes in cloud forcing due to 4xCO₂, corrected for cloud masking effects. Error bars are estimated from ω changes in year 1 and year 2 computed separately.

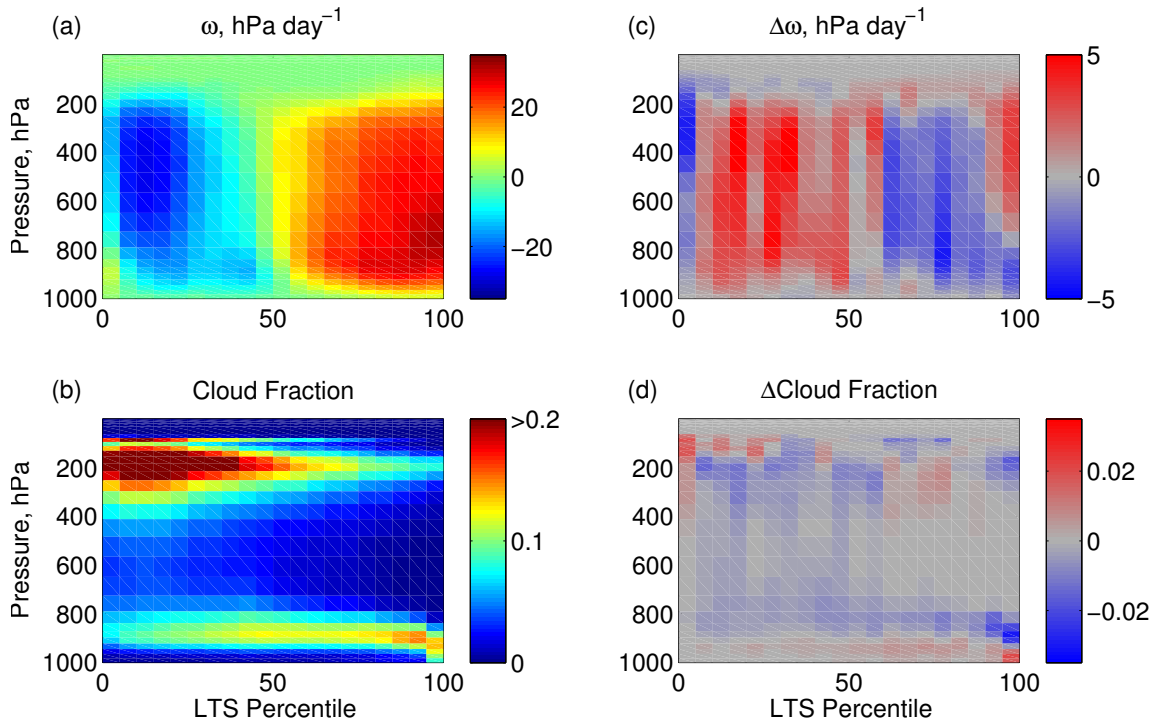


Figure 11: Monthly-mean tropical ocean profiles sorted by LTS for the SP-CAM. Control case (a) 500 hPa pressure velocity ω and (b) cloud fraction, and corresponding 4xCO₂ changes, (c)-(d).

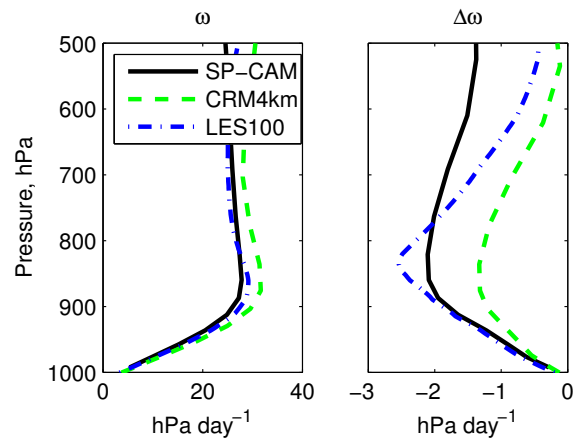


Figure 12: Pressure velocity ω (left) and the difference in ω for the 4xCO₂ case, $\Delta\omega$ (right), for SP-CAM LTS 80-90th percentile, CRM4km, and LES100.

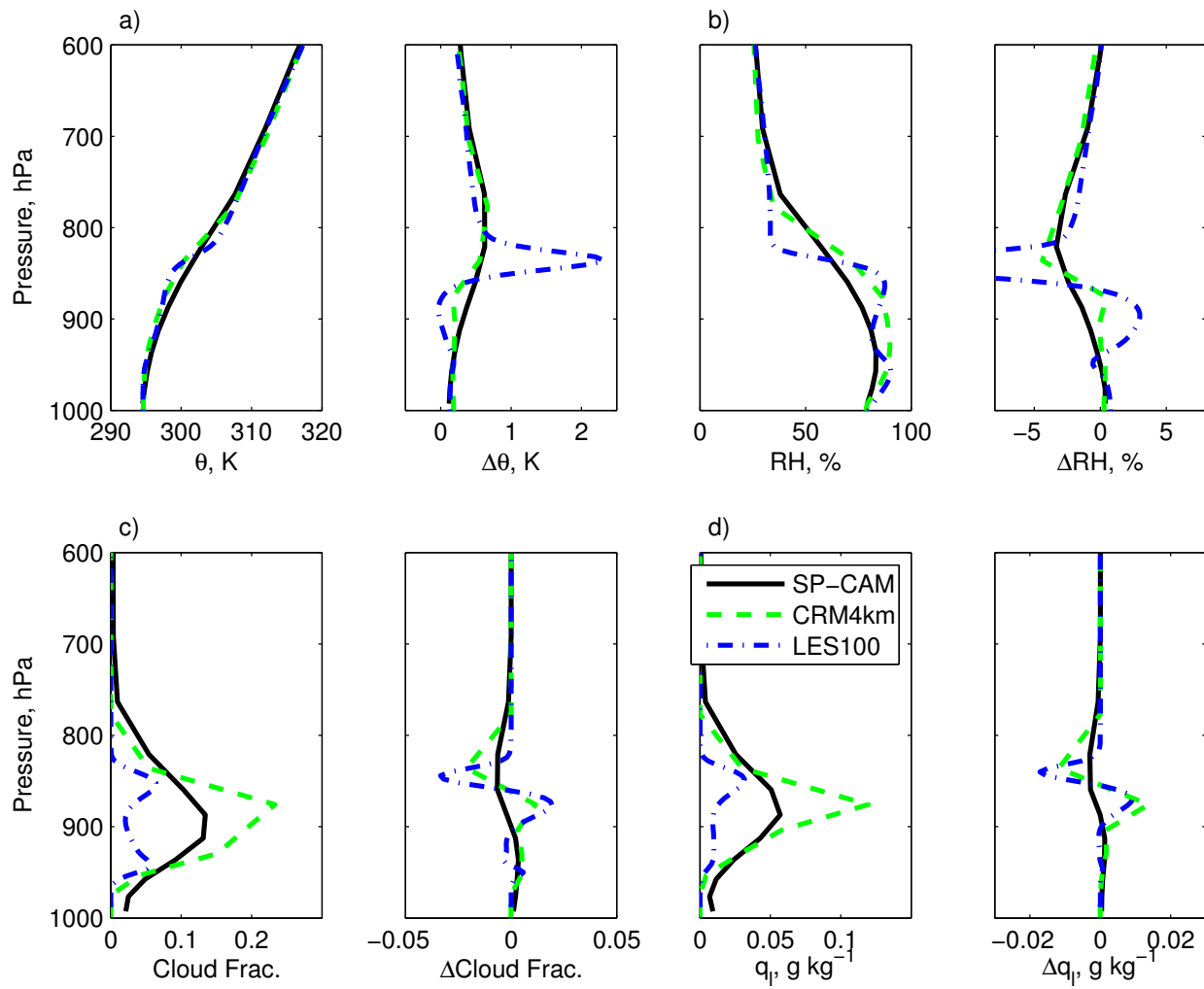


Figure 13: Comparison of SP-CAM, CRM4km, and LES100 profiles of a) potential temperature (K), b) relative humidity, c) cloud fraction, and d) cloud liquid water (g kg^{-1}) for the control (left) and the change with 4xCO₂ (right). At the MBL inversion, the LES100 profile of Δ RH in b) goes off the the displayed horizontal scale and extends to -27%.

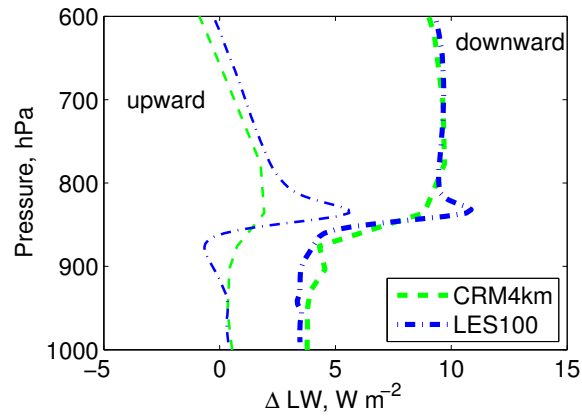


Figure 14: $4xCO_2$ changes in upward (thin) and downward (thick) radiative flux (in $W m^{-2}$) for LTS80-90 CRM4km (blue dashed) and LES100 (green dash-dot) simulations.

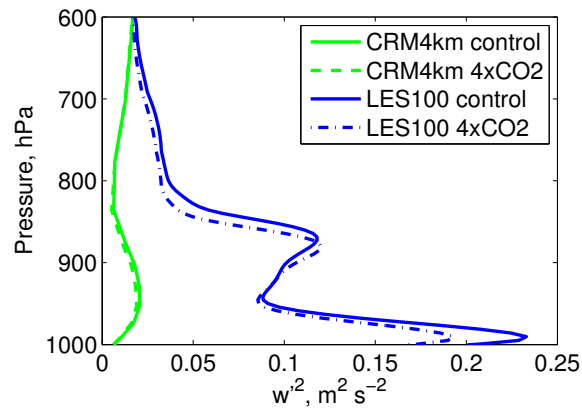


Figure 15: Vertical velocity variance $\overline{w'^2}$ for LTS80-90 CRM4km and LES100 control and $4xCO_2$ simulations in $m^2 s^{-2}$.